nature geoscience

Article

https://doi.org/10.1038/s41561-023-01332-x

Atmospheric methane variability through the Last Glacial Maximum and deglaciation mainly controlled by tropical sources

Received: 27 January 2023

Accepted: 20 October 2023

Published online: 27 November 2023



Check for updates

Ben Riddell-Young ®¹⊠, Julia Rosen¹, Edward Brook¹⊠, Christo Buizert¹, Kaden Martin 1, James Lee 2, Jon Edwards, Michaela Mühl 3, Jochen Schmitt 93, Hubertus Fischer 93 & Thomas Blunier 94

Constraining the causes of past atmospheric methane variability is important for understanding links between methane and climate. Abrupt methane changes during the last deglaciation have been intensely studied for this purpose, but the relative importance of high-latitude and tropical sources remains poorly constrained. The methane interpolar concentration difference reflects past geographic emission variability, but existing records suffered from subtle but considerable methane production during analysis. Here, we report an ice-core-derived interpolar difference record covering the Last Glacial Maximum and deglaciation, with substantially improved temporal resolution, chronology and a critical correction for methane production in samples from Greenland. Using box models to infer latitudinal source changes, we show that tropical sources dominated abrupt methane variability of the deglaciation, highlighting their sensitivity to abrupt climate change and rapidly shifting tropical rainfall patterns. Northern extratropical emissions began increasing ~16,000 years ago, probably through wetland expansion and/or permafrost degradation induced by high-latitude warming, and contributed at most 25 Tg yr⁻¹ (45% of the total emission increase) to the abrupt methane rise that coincided with rapid northern warming at the onset of the Bølling-Allerød interval. These constraints on deglacial climate-methane cycle interactions can improve the understanding of possible present and future feedbacks.

Methane (CH₄) is a potent greenhouse gas. Predominantly anthropogenic CH₄ emissions have nearly tripled the atmospheric mixing ratio ([CH₄]) from preindustrial values¹, with record growth rates in the past few years linked to tropical sources². Large uncertainties in future CH₄ climate forcing stem from a range of anthropogenic emission pathways and poorly constrained natural emission responses to changing climate³. Fears that warming will trigger rapid releases of ancient CH₄ trapped in high-latitude permafrost⁴ and/or marine and subglacial clathrates⁵ have received substantial attention, but positive feedbacks have also been proposed for tropical microbial CH₄ emissions^{6,7}. Uncertainties surrounding these feedbacks can be reduced using studies of past [CH₄] variability.

Ancient air in ice cores has revealed that past [CH4] fluctuated between ~350 and ~800 parts per billion (ppb) over the past 800,000

¹College of Earth, Ocean, and Atmospheric Sciences, Oregon State University, Corvallis, OR, USA. ²Los Alamos National Laboratory, Los Alamos, NM, USA. 3Climate and Environmental Physics, Physics Institute, and Oeschger Centre for Climate Change Research, University of Bern, Bern, Switzerland. ⁴Center for Ice and Climate, University of Copenhagen, Copenhagen, Denmark. 🖂 e-mail: riddellb@oregonsate.edu; Edward.Brook@oregonstate.edu years $^{8-11}$. During glacial periods, [CH₄] varied abruptly, with decadal-to centennial-scale shifts of 5 0–250 ppb 9,10,12,13 that closely followed the abrupt, millennial-scale Northern Hemisphere (NH) climate transitions of the Dansgaard–Oeschger (DO) cycle 9,14 . This linkage has been attributed to shifts in the meridional position and regional strength of tropical rain belts in response to abrupt NH climate change, impacting tropical wetland CH₄ emissions 8,9,15,16 .

[CH₄] variability during the Last Glacial Maximum (LGM) and deglaciation captures the full glacial-interglacial range and millennialscale features such as Heinrich Stadials 2b, 2a and 1 (HS2b, HS2a and HS1, respectively), the Bølling-Allerød Warming (BA) and the Younger Dryas cold interval (YD)¹⁷. The stable isotopic composition of atmospheric CH₄ (δD-CH₄ and δ¹³C-CH₄) reflects contributions from different source types and sinks¹⁸⁻²¹, and suggests that both orbitaland millennial-scale [CH₄] variability was largely driven by changes in microbial (primarily wetland) rather than geologic or pyrogenic emissions^{11,15,19,20,22,23}. Interpretations, particularly distinctions between tropical and high-latitude microbial emissions, are complicated by potential temporal variability in the atmospheric sink fractionation factor and isotopic source signatures^{11,15,21,24}. The radiocarbon content (14C) of atmospheric CH₄ reflects the contribution of geologic (14C-free) CH₄ sources, such marine clathrates or fossil seeps. 14C data indicate that geologic emissions were small during the Holocene²⁵ (<5.4 Tg yr⁻¹) and contributed to less than 10% of the deglacial [CH₄] rise²², although a noteworthy contribution of permafrost-derived CH₄ cannot be ruled out^{22,23}.

Stable isotope and ^{14}C results 22 agree with Earth-system modelling studies, which suggest wetland emission changes were large enough to explain the observed deglacial [CH₄] change $^{26\text{-}28}$. However, we have limited knowledge of which wetland regions were most influential. The [CH₄] interpolar difference (IPD) can be used to constrain the latitudinal distribution of CH₄ sources. The relative IPD (rIPD) is normalized for [CH₄] change and is defined as:

$$rIPD = \left(\frac{CH_{4,N}}{CH_{4,S}} - 1\right) \times 100\% \tag{1}$$

where $CH_{4,N}$ is Arctic $[CH_4]$ and $CH_{4,S}$ is Antarctic $[CH_4]^{29}$. Positive or negative changes in the rIPD indicate net northward or southward shifts of sources, respectively, assuming variables such as atmospheric lifetime and interhemispheric mixing times remain constant (Methods).

Previous work reconstructed the past rIPD by measuring the difference between synchronized [CH₄] records from Greenland and Antarctic ice cores $^{9,12,29-34}$. This work was challenging due to sparse sampling, imprecise ice-core age scale synchronization and measurement uncertainties. Further, previous studies pre-date the recognition of non-atmospheric CH₄ release during the commonly used wet-extraction analysis method 35 . This excess methane (CH_{4xs}) ranges from 5 to 40 ppb and is strongly correlated with the non-sea-salt calcium (Ca $^{2+}$) content of the ice, a common proxy for dust 36 . Because CH_{4xs} is only found in Greenland ice during high-Ca $^{2+}$ stadial periods, published rIPD reconstructions consequently overestimated the rIPD, and thus the contribution of northern extratropical sources to the CH₄ budget, during these stadials.

We present a reconstruction of the CH_4 rIPD from 27.5 to 11.6 kyr ago (ka) using $[CH_4]$ data from the North Greenland Eemian (NEEM), Greenland Ice Sheet Project phase 2 (GISP2) and West Antarctic Ice Sheet Divide (WD) ice cores (Fig. 1 and Table 1). The NEEM and GISP2 $[CH_4]$ data were smoothed and synchronized to the smoothed WD $[CH_4]$ data to calculate independent records of the rIPD (Fig. 2). Our results improve on previous efforts in two ways. First, a considerable increase in temporal resolution and measurement precision permits improved synchronization of the Antarctic and Greenland $[CH_4]$ records. This allows rIPD reconstruction at sub-millennial resolution. Second, we reconstruct the true rIPD by correcting for CH_{4xs} (Fig. 2). A four-box troposphere model is used to interpret the rIPD (Fig. 3) and its sensitivity

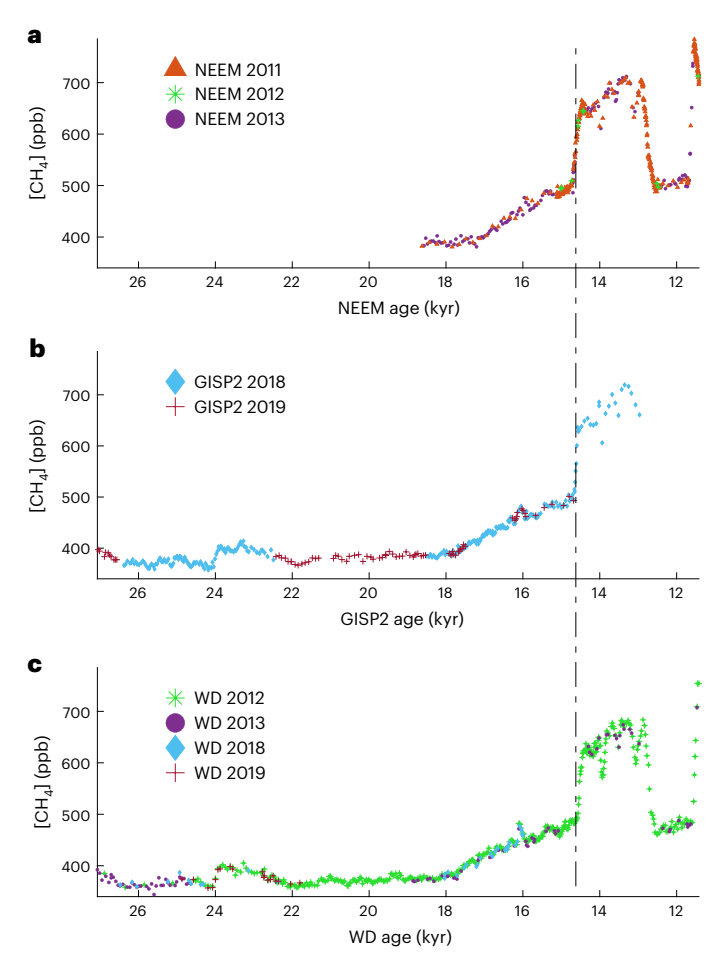


Fig. 1| **Summary of all discrete-sample CH**₄ **data and corrections used in this study.** \mathbf{a} – \mathbf{c} , NEEM (\mathbf{a}), GISP2 (\mathbf{b}) and WD (\mathbf{c}) CH₄ data plotted on their original gas age scale chronologies, coloured by measurement campaign. The data are blank, solubility, gravity and analytical campaign offset-corrected. The Greenland data (NEEM and GISP2) are also corrected for CH_{4xs}. Colours and symbols correspond to the year samples were measured (see legend). The vertical dashed line at the HS1–BA [CH₄] rise, which should be synchronous in each core, demonstrates the small disagreements between the three independently developed gas age scale chronologies that we correct for in our synchronization (Methods).

to variables other than changes in total tropical and northern extratropical source strength (Methods) 9,29 . We show that tropical sources dominated abrupt, millennial-scale CH₄ variability, while northern extratropical sources played an influential but secondary role in the deglacial [CH₄] rise.

CH₄ IPD trends of the LGM and deglaciation

The rIPD varied between 0 and 6% from 27.5 to 11.6 ka (Holocene onset). Correcting for CH_{4xs} greatly decreased both the NEEM- and GISP2-derived rIPDs in key stadial intervals with high Ca^{2+} . Because our uncorrected rIPD agrees with previous studies (Fig. 2, Supplementary Information Section 6 and Supplementary Table 4), we suspect that CH_{4xs} impacted all previous CH_4 records from Ca^{2+} -rich Greenland samples measured using discrete melt-extraction systems.

Our CH_{4xs} -corrected record reveals new trends in the rIPD across the deglaciation. First, we find that the rIPD was lowest (0-1%) during HS2a and HS1. Second, we find a 5 percentage point increase in the rIPD from mid-HS1 to the YD. Multi-centennial-scale agreement between the GISP2- and NEEM-derived rIPD reconstructions, which overlap from 18.5 to 14.5 ka, is excellent, suggesting that interpretations of our rIPD at sub-millennial timescales are robust (Fig. 3a). These results are discussed in detail for specific time intervals below.

GISP2

GISP2

+3.9

+4.0

Core	Year	No. samples (duplicates)	Duplicate pooled s.d.	Blank correction (ppb)	Solubility correction (%)	Average gravitational fractionation correction (%)	2013 offset (ppb)	Offset s.d. (ppb)
NEEM	2010 2011	496 (315)	4.3	-8.8	+1.4	+0.39	-1.2	7.8
NEEM	2012	14 (0)		-8.9	+1.4	+0.39	-1.2	7.8
NEEM	2013	130 (106)	2.8	-7.5	+1.4	+0.39		
WD	2012	518 (313)	1.6	-8.9	+1.7	+0.36	0.1	3.9
WD	2013	99 (99)	2.0	-7.5	+1.4	+0.36		
WD	2018	65 (9)	3.4	-7.8	+1.7	+0.36	+3.9	5.3
WD	2019	20 (6)		-73	+1 7	+0.36	+40	<i>A</i> 1

+1.7

+1.7

Table 1| Summary of the corrections made to CH₄ data from each ice core and corresponding measurement campaign

Shown from left to right are the total number of samples and duplicate measurements in parentheses, duplicate pooled standard deviation (s.d.), blank correction, solubility correction, average gravitational fractionation correction, and offset correction and its standard deviation applied to each sample group relative to the 2013 measurement campaign. The sign of the correction represents whether the correction increased (+) or decreased (-) the [CH₄].

HS2 and LGM

2018

2019

At the start of our record, the rIPD gradually decreased from ~2% to a minimum of 0% at the onset of HS2a (Fig. 3a), when [CH₄] abruptly increased by 40 ppb. Box-modelled total tropical emissions, primarily comprising microbial wetland sources $^{1.37-39}$, increased by 20 Tg yr $^{-1}$, to 105 Tg yr $^{-1}$, across this [CH₄] rise, while northern extratropical emissions decreased to a minimum of 5 Tg yr $^{-1}$ (Fig. 3e). In our four-box model, we assumed equal northern and southern tropical emissions. Tests exploring the sensitivity of this assumption to our analyses (Methods) indicate that a shift of only ~10% of total tropical emissions from north to south of the equatorial barrier to interhemispheric mixing is necessary to reproduce the observed rIPD drop between HS2b and HS2a. Had such a shift occurred, the assumption of equal northern and southern tropical emissions would have caused an overestimate of the influence of total tropical sources on the HS2a [CH₄] increase by up to 5 Tg yr $^{-1}$ (Methods).

253 (169)

276 (175)

3.1

3.4

-7.8

-7.3

In fact, a southward shift of tropical CH₄ emissions during HS2a is supported by proxy evidence of weak monsoon conditions across the NH tropics and mid-latitudes (Fig. 3c)^{40,41}. Coincident intensification of precipitation across the southern tropics may have expanded wetland extent and enhanced microbial CH₄ emissions there, counteracting emission decreases in the drying NH tropics 42,43. Further, the abrupt, centennial-scale [CH₄] features found within HS intervals have been attributed to enhanced southern tropical wetland CH₄ emissions driven by southerly precipitation shifts 41,44. In contrast, the rIPD, [CH₄] and box-modelled emissions remained stable during HS2b. Proxy evidence indicates that HS2b was weaker than HS2a (Fig. 3c)40,45,46 with less extensive increases in southern tropical rainfall and wetland emissions. The contrast in emission patterns between HS2a and HS2b, consistent with proxy evidence of the relative strength of each event, suggests that climate variability associated with Heinrich stadials contemporaneously regulated the latitudinal distribution and strength of sources, and thus [CH4].

The short-lived Dansgaard–Oeschger 2 (DO2) interstadial was characterized by NH warming 47 , a northward shift of tropical rain belts 48 , but minimal change in [CH4]. At face value, our four-box model suggests that decreasing tropical emissions and increasing northern extratropical emissions caused the -4 percentage point rIPD increase between HS2a and DO2 (Fig. 3). This is contrary to the longstanding hypothesis that DO interstadials were associated with enhanced tropical CH4 emissions driven by rainfall migrating northward to more wetland-prone regions 9,16,29 . Increased northern extratropical emissions during DO2 are also unlikely, given low NH insolation 49 and maximum NH ice-sheet extent 50 . More likely, a northward tropical emission shift, evidenced by the northward migration of tropical rain belts 40 , increased

the rIPD without changing net emissions or the proportion of northern extratropical to total tropical emissions (Methods). From DO2 to the HS1 onset, [CH₄], the rIPD, and modelled tropical and northern extratropical emissions remained relatively stable at 390 ppb, 3%, 85 Tg yr⁻¹ and 20 Tg yr⁻¹, respectively. Our interpretation that tropical wetland CH₄ emissions, modulated by millennial-scale climate variability, were the primary regulator of [CH₄] change during this interval is supported by CH₄ stable isotope ^{11,21} and Earth-system modelling studies ^{16,28,39}.

+0.44

+0.44

HS1

The GISP2- and NEEM-derived rIPDs were ~3% at the start of HS1, decreased to 0–1% and increased again to ~3% by the end of HS1. Unlike HS2a, [CH4] gradually increased by 100 ppb during HS1, which our box model attributes primarily to a 25 Tg yr $^{-1}$ increase in tropical emissions. This rIPD decrease but tropical emissions increase is probably due to the impacts of the southward migration of tropical rain belts associated with HS1 superimposed on longer-term increasing global temperatures and fertilization effects through rising [CO2] during the deglaciation 27,28 . Precession-driven increases in NH tropical summer insolation may have also enhanced HS1 tropical wetland activity (Fig. 3a) 38,51 .

HS1 rIPD trends also provide insight into contemporaneous changes to CH_4 biogeochemistry in boreal regions. Box-modelled northern extratropical emissions began rising -16 ka and increased by $10\,\text{Tg}\,\text{yr}^{-1}$ by the end of HS1. However, our interpretations of the precise timing of this onset and magnitude of the rise are within the uncertainty bounds of our box model and sensitive to unconstrained latitudinal shifts in tropical emissions within HS1 that may have impacted the rIPD. Nonetheless, the rIPD provides indirect, top-down evidence of the onset of enhancing northern extratropical microbial CH_4 emissions during the deglaciation, probably driven by increasing NH summer insolation, early NH ice-sheet retreat and increasing global temperatures 28,38,51,52 .

The BA and YD

The HS1–BA transition (14.6 ka) was characterized by an abrupt increase in Greenland temperature 47,53 and a rapid, -150 ppb [CH $_4$] rise 8,38 . The BA–YD transition (12.8 ka) occurred 2 kyr later with equally abrupt decreases in [CH $_4$] and Greenland temperature 47 . From the start of the BA to the end of our record 11.6 ka, the rIPD gradually increased from 3 to 6% (Fig. 3a), providing constraints on the high-latitude contribution to the deglacial [CH $_4$] rise.

At the HS1–BA transition, box-modelled CH $_4$ emissions increased by 30 Tg yr $^{-1}$ in the tropics and 25 Tg yr $^{-1}$ in the northern extratropics. As above, the model assumes equal contributions from the northern and southern tropics, but proxies suggest enhanced northern tropical

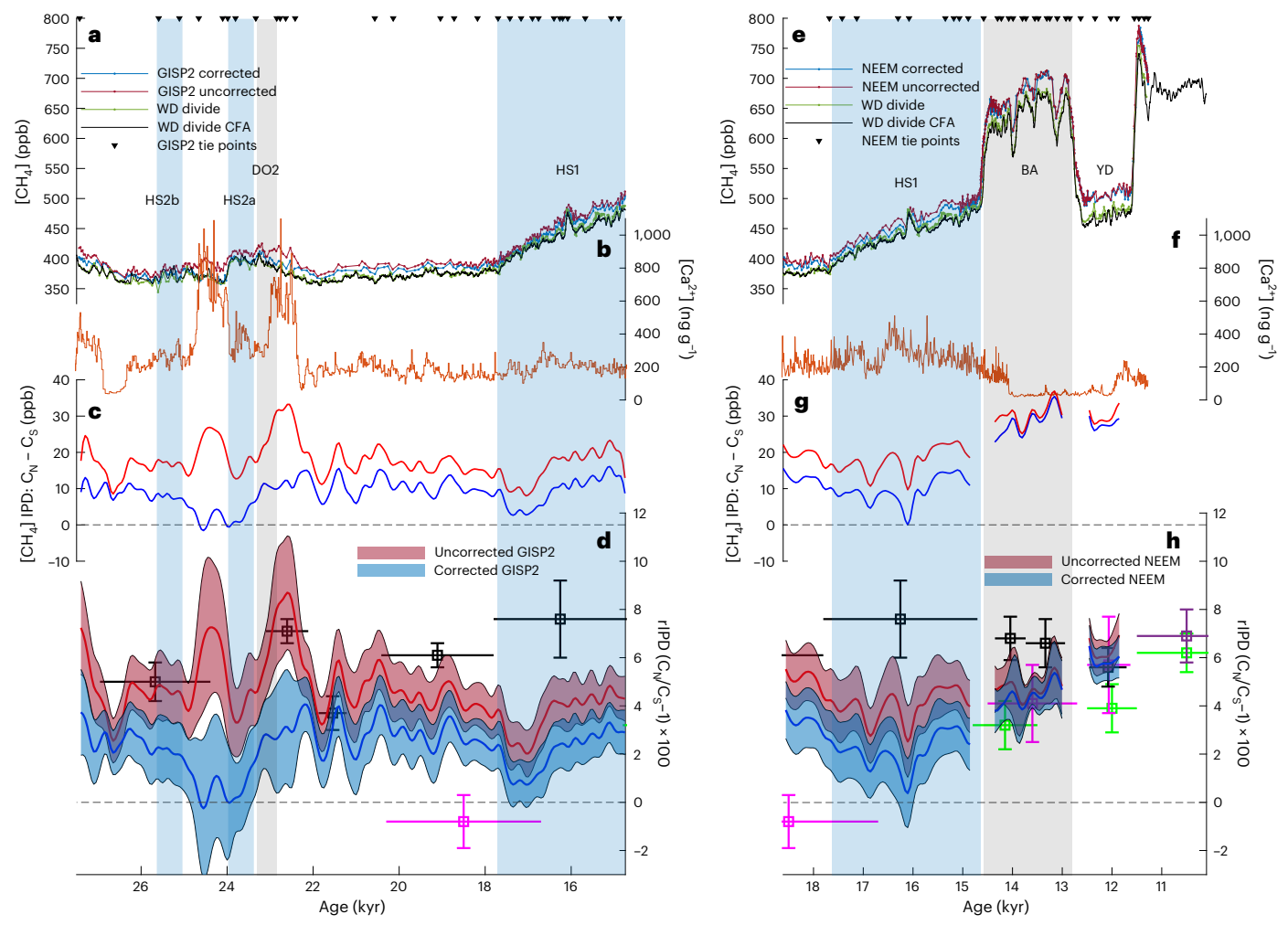


Fig. 2 | The CH₄ rIPD records derived using GISP2 and NEEM. a,e, Tie points (black triangles), CH_{4xs}-corrected (blue) and -uncorrected (red) discrete Greenland [CH₄] records (a: GISP2, e: NEEM), discrete WD [CH₄] record (green), and WD continuous flow analysis (CFA) [CH₄] record (black)⁶¹. The WD CFA record is shown for visual aid when discrete data are not available. b, f, The [Ca²⁺] record for GISP2 (b)⁶² and NEEM (f)⁶³ plotted on each core's WD-synchronized gas age scales (orange). c,g, IPD measurements corrected (blue) and uncorrected (red) for CH_{4xs} derived using GISP2 (c) and NEEM (g). d,h, rIPD measurements

corrected (blue) and uncorrected (red) for CH_{4xs} and their 95% confidence intervals derived using GISP2 (**d**) and NEEM (**h**). In the NEEM-derived rIPD, abrupt transitions in $[CH_4]$ where the rIPD is not well defined are not shown in **g** and **h**. We suspect that the abrupt oscillations in the rIPD from 22 to 21 ka are an artefact of our analysis and are caused by a brief lack of available tie points and low data resolution. The interval-averaged rIPD estimates from previous studies are plotted in black¹², green⁹, purple²⁹ and magenta³¹. Heinrich stadial^{45,64} and DO interstadial¹⁷ climate intervals are shaded in light blue and grey, respectively.

rainfall associated with northern warming 40,41 . A resulting shift of emissions to the northern tropics would have increased the rIPD, causing our box model to overestimate northern extratropical emissions by up to $10~{\rm Tg\,yr^{-1}}$ (Supplementary Fig. 10). Our rIPD thus provides strong evidence that northern extratropical sources contributed at most 45% of the global CH $_4$ source increase across the HS1–BA transition [CH $_4$] rise (15–25 Tg yr $^{-1}$ of the cumulative 55 Tg yr $^{-1}$ increase in emissions). CH $_4$ stable isotope records show minimal change across the HS1–BA transition 11,19,21 , and 14 C data imply limited contributions from geologic sources 22,23 , supporting the hypothesis that tropical wetland emissions dominated the [CH $_4$] increase.

Our four-box model attributes the 200 ppb decrease in $[CH_4]$ across the BA-YD transition to a modest 5 Tg yr $^{-1}$ drop in northern extratropical emissions and large -50 Tg yr $^{-1}$ drop in tropical emissions, in agreement with recent Earth-system modelling estimates 54 . Abrupt NH cooling probably caused a southward displacement of tropical rain belts and net drying of tropical wetland regions (Fig. 3c) 8,14,55 . The resulting southward shift of tropical emissions during the BA-YD transition would have violated the assumption of equal southern and northern tropical emissions, causing our box model to overestimate

YD tropical emissions and underestimate northern extratropical emissions, each by up to $10~{\rm Tg\,yr^{-1}}$ (Supplementary Fig. 10). Therefore, it is probable that northern extratropical emissions remained relatively stable across this transition, despite the dramatic drop in [CH₄] and considerable NH cooling ^{50,56}, presumably because YD cooling mainly affected temperatures during winter rather than summer when most CH₄ emissions occurred ^{56,57}.

Proxy evidence suggests that the latitudinal distribution of tropical precipitation during HS1 and the YD was similar 40,41,55 , so the observed rIPD difference between these two intervals was probably driven by enhanced northern extratropical and reduced total tropical emissions, not latitudinal shifts in the tropical source. This suggests that our box-modelled $15\,\mathrm{Tg}\,\mathrm{yr}^{-1}$ decrease in tropical emissions between the end of HS1 and the YD is accurate, despite similar [CH₄] and weak regional drying in wetland-prone regions during the YD (Fig. 3c.) 40,55 . Additionally, NH tropical summer insolation (Fig. 3a), global average temperatures and [CO₂] all increased from HS1 values; each thought to cause enhanced wetland CH₄ emissions and increased [CH₄] 38,51 . The considerable 40 m of sea level rise between HS1 and the YD (Fig. 3d) 58 may explain the reduced YD tropical emissions relative to HS1. The

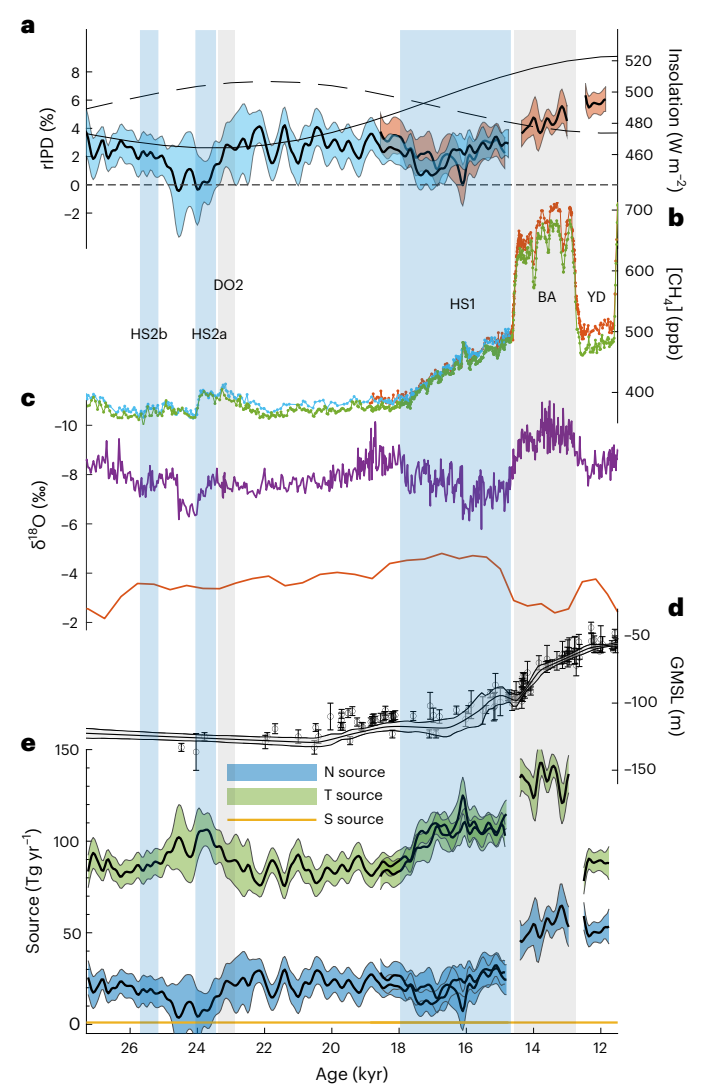


Fig. 3 | **Four-box-model results for the NEEM- and GISP2-derived rIPDs. a**, NEEM (orange) and GISP2 (light blue) rIPDs (mean of Monte Carlo analysis), each plotted with 95% confidence intervals, as well as insolation curves for 60° N in June (solid black curve) and 30° S in December (dashed black curve)⁴⁹. **b**, The CH_{4xs}-corrected [CH₄] records for NEEM (orange), GISP2 (light blue) and WD (green). **c**, Speleothem-derived δ¹⁸O records for Botuverà Cave in Brazil (27° 13′ S; orange)⁴² and a composite of Chinese records (32° 30′ N; purple)⁴⁰. **d**, Global mean sea level (GMSL) data (squares) and model results (curve)⁵⁸, each plotted with 1σ uncertainty. **e**, CH₄ rIPD box-model results: source strengths for the northern extratropical (N; blue), total tropical (T; green) and southern extratropical (S; yellow) boxes and their 95% confidence interval uncertainties. In the NEEM-derived rIPD, abrupt transitions in [CH₄] where the rIPD and box-modelled emissions are untrustworthy are not shown (**a** and **e**). Heinrich stadial^{45,64} and DO interstadial¹⁷ climate intervals are shaded in light blue and grey, respectively.

resulting extensive saltwater inundation of low-elevation floodplains, such as the Sunda Shelf, may have reduced net tropical wetland productivity and CH₄ emissions ^{11,26,54}. Increased southern tropical rainfall during the YD⁵⁵ may have also been too weak to stimulate wetland emissions capable of counteracting reduced emissions from the drying northern tropics.

Although our rIPD reconstruction does not continue into the early Holocene due to limited discrete WD [CH₄] data (Methods), we find it probable that the abrupt ~250 ppb [CH₄] increase at the YD–Holocene transition was also driven by enhanced net tropical wetland emissions due to an abrupt northward shift of tropical rain belts 40 . Existing rIPD data from the early Holocene indicate that the rIPD was ~6% $^{9.29,33,34}$

(Fig. 2h), a value not impacted by CH_{4xs} due to low Ca^{2+} in Greenland Holocene ice³⁶. Coupled with our YD rIPD of 6%, this indicates a relatively stable rIPD across the YD–Holocene transition. Thus, the proportion of tropical to northern extratropical emissions probably changed little and increased tropical CH_4 emissions drove the abrupt $[CH_4]$ rise at this transition. This is consistent with interpretations of CH_4 stable isotope and radiocarbon data^{11,19,21,22}.

Box-modelled northern extratropical emissions increased by 25 Tg yr $^{-1}$ from HS1 to the end of the YD. This could be explained by expansions of CH $_4$ -emitting boreal wetlands and intensifying CH $_4$ emissions from permafrost degradation following the rapid retreat of NH ice sheets during the deglaciation and subsequent warming 52,59 . The fertilization effect of rising [CO $_2$] during the deglaciation may have further enhanced northern extratropical microbial emissions 27,28 . This 25 Tg yr $^{-1}$ increase is well within ^{14}C -derived estimates of permafrost emissions, which place a -50 Tg yr $^{-1}$ upper limit on the contribution of this source to the deglacial [CH $_4$] rise 22 . Furthermore, northern extratropical summer insolation began increasing 21 ka (Fig. 3a), which possibly enhanced already increasing boreal wetland productivity from accelerating NH ice-sheet retreat 38,49 . These trends in deglacial northern extratropical emissions agree well with Earth-system modelling studies 16,28,60 , which suggest a secondary role of high-latitude NH microbial emissions 19,21 .

The ice-core-derived CH₄ rIPD record presented here provides insight into the timing and geographic distribution of the major terrestrial biogeochemical changes of the LGM and deglaciation. Our CH_{4xs}-corrected record reveals rIPD values near 0% during Heinrich stadials and a large increase across the deglaciation. Box-model analyses indicate that tropical sources dominated the CH₄ budget and mainly controlled abrupt millennial-scale [CH₄] variability for much of the record, with northern extratropical sources playing an influential but secondary role in the deglacial [CH₄] rise. Sensitivity tests reveal that variables other than changes in the ratio of tropical to northern extratropical emissions could explain some of the observed variability in the rIPD, but cannot provide alternative explanations of the general drivers of LGM and deglacial [CH₄] variability.

We suggest that increasing northern extratropical emissions beginning -16 ka were driven by wetland expansion and/or permafrost degradation induced by accelerating ice-sheet retreat, increasing NH summer insolation and rising temperatures. On the millennial scale, the migration of tropical rain belts and monsoon intensity induced by abrupt NH climate variability rapidly modulated tropical wetland productivity and, consequentially, tropical CH_4 emissions and $[CH_4]$. We place an upper, $25\,Tg\,yr^{-1}$ limit on the northern extratropical contribution to the rapid HS1–BA $[CH_4]$ rise; 45% of the total increase in emissions. Although noteworthy, this change is small with respect to the modern CH_4 budget 1 . Instead, the dominant tropical role underscores the sensitivity of tropical microbial CH_4 emissions to rapid climate and hydrological change, and the need to better understand how this relationship will modify future emissions at a time when annual emissions continue to rapidly increase 2 .

Online content

Any methods, additional references, Nature Portfolio reporting summaries, source data, extended data, supplementary information, acknowledgements, peer review information; details of author contributions and competing interests; and statements of data and code availability are available at https://doi.org/10.1038/s41561-023-01332-x.

References

- Saunois, M. et al. The global methane budget 2000–2017. *Earth Syst. Sci. Data* 12, 1561–1623 (2020).
- Feng, L., Palmer, P. I., Parker, R. J., Lunt, M. F. & Bösch, H. Methane emissions are predominantly responsible for recordbreaking atmospheric methane growth rates in 2020 and 2021. Atmos. Chem. Phys. 23, 4863–4880 (2023).

- 3. Dean, J. F. et al. Methane feedbacks to the global climate system in a warmer world. *Rev. Geophys.* **56**, 207–250 (2018).
- Schuur, E. A. et al. Climate change and the permafrost carbon feedback. Nature 520, 171–179 (2015).
- Ruppel, C. D. & Kessler, J. D. The interaction of climate change and methane hydrates. Rev. Geophys. 55, 126–168 (2017).
- Cheng, C.-H. & Redfern, S. A. Impact of interannual and multidecadal trends on methane-climate feedbacks and sensitivity. *Nat. Commun.* 13, 3592 (2022).
- Kleinen, T., Gromov, S., Steil, B. & Brovkin, V. Atmospheric methane underestimated in future climate projections. *Environ. Res. Lett.* 16, 094006 (2021).
- Chappellaz, J., Barnola, J., Raynaud, D., Korotkevich, Y. S. & Lorius, C. Ice-core record of atmospheric methane over the past 160,000 years. *Nature* 345, 127–131 (1990).
- Brook, E. J., Harder, S., Severinghaus, J., Steig, E. J. & Sucher, C. M. On the origin and timing of rapid changes in atmospheric methane during the last glacial period. *Glob. Biogeochem. Cycles* 14, 559–572 (2000).
- Loulergue, L. et al. Orbital and millennial-scale features of atmospheric CH₄ over the past 800,000 years. Nature 453, 383–386 (2008).
- Bock, M. et al. Glacial/interglacial wetland, biomass burning, and geologic methane emissions constrained by dual stable isotopic CH₄ ice core records. Proc. Natl Acad. Sci. USA 114, E5778–E5786 (2017).
- Baumgartner, M. et al. High-resolution interpolar difference of atmospheric methane around the Last Glacial Maximum. Biogeosciences 9, 3961–3977 (2012).
- Buizert, C. et al. The WAIS divide deep ice core WD2014 chronology—part 1: methane synchronization (68–31 ka BP) and the gas age-ice age difference. Clim. Past 11, 153-173 (2015).
- Brook, E. J., Harder, S., Severinghaus, J. & Bender, M. Atmospheric methane and millennial-scale climate change. *Geophys. Monogr.* Ser. 112, 165–176 (1999).
- 15. Möller, L. et al. Independent variations of CH_4 emissions and isotopic composition over the past 160,000 years. *Nat. Geosci.* **6**, 885–890 (2013).
- Hopcroft, P. O., Valdes, P. J., O'Connor, F. M., Kaplan, J. O. & Beerling, D. J. Understanding the glacial methane cycle. Nat. Commun. 8, 14383 (2017).
- Rasmussen, S. O. et al. A stratigraphic framework for abrupt climatic changes during the last glacial period based on three synchronized Greenland ice-core records: refining and extending the INTIMATE event stratigraphy. Quat. Sci. Rev. 106, 14–28 (2014).
- Sherwood, O. A., Schwietzke, S., Arling, V. A. & Etiope, G. Global inventory of gas geochemistry data from fossil fuel, microbial and burning sources, version 2017. Earth Syst. Sci. Data 9, 639–656 (2017).
- Sowers, T. Late quaternary atmospheric CH₄ isotope record suggests marine clathrates are stable. Science 311, 838–840 (2006)
- 20. Bock, M. et al. Hydrogen isotopes preclude marine hydrate ${\rm CH_4}$ emissions at the onset of Dansgaard–Oeschger events. *Science* **328**, 1686–1689 (2010).
- Fischer, H. et al. Changing boreal methane sources and constant biomass burning during the last termination. *Nature* 452, 864–867 (2008).
- Dyonisius, M. et al. Old carbon reservoirs were not important in the deglacial methane budget. Science 367, 907–910 (2020).
- Petrenko, V. V. et al. Minimal geological methane emissions during the Younger Dryas–Preboreal abrupt warming event. *Nature* 548, 443–446 (2017).

- Levine, J., Wolff, E., Hopcroft, P. O. & Valdes, P. J. Controls on the tropospheric oxidizing capacity during an idealized Dansgaard– Oeschger event, and their implications for the rapid rises in atmospheric methane during the last glacial period. *Geophys. Res. Lett.* 39, L12805 (2012).
- 25. Hmiel, B. et al. Preindustrial ¹⁴CH₄ indicates greater anthropogenic fossil CH₄ emissions. *Nature* **578**, 409–412 (2020).
- Weber, S., Drury, A., Toonen, W. & Van Weele, M. Wetland methane emissions during the Last Glacial Maximum estimated from PMIP2 simulations: climate, vegetation, and geographic controls. *J. Geophys. Res. Atmos.* 115, D06111 (2010).
- Ringeval, B. et al. Response of methane emissions from wetlands to the Last Glacial Maximum and an idealized Dansgaard– Oeschger climate event: insights from two models of different complexity. Climate 9, 149–171 (2013).
- Kleinen, T., Mikolajewicz, U. & Brovkin, V. Terrestrial methane emissions from the Last Glacial Maximum to the preindustrial period. Climate 16, 575–595 (2020).
- 29. Chappellaz, J. et al. Changes in the atmospheric CH_4 gradient between Greenland and Antarctica during the Holocene. J. Geophys. Res. Atmos. **102**, 15987–15997 (1997).
- Rasmussen, R. A. & Khalil, M. Atmospheric methane in the recent and ancient atmospheres: concentrations, trends, and interhemispheric gradient. J. Geophys. Res. Atmos. 89, 11599–11605 (1984).
- 31. Dällenbach, A. et al. Changes in the atmospheric CH_4 gradient between Greenland and Antarctica during the Last Glacial and the transition to the Holocene. *Geophys. Res. Lett.* **27**, 1005–1008 (2000).
- 32. Mitchell, L., Brook, E., Lee, J. E., Buizert, C. & Sowers, T. Constraints on the late Holocene anthropogenic contribution to the atmospheric methane budget. *Science* **342**, 964–966 (2013).
- 33. Beck, J. et al. Bipolar carbon and hydrogen isotope constraints on the Holocene methane budget. *Biogeosciences* **15**, 7155–7175 (2018).
- 34. Yang, J.-W., Ahn, J., Brook, E. J. & Ryu, Y. Atmospheric methane control mechanisms during the early Holocene. *Climate* **13**, 1227–1242 (2017).
- Lee, J. E. et al. Excess methane in Greenland ice cores associated with high dust concentrations. Geochim. Cosmochim. Acta 270, 409–430 (2020).
- 36. Legrand, M., Lorius, C., Barkov, N. & Petrov, V. Vostok (Antarctica) ice core: atmospheric chemistry changes over the last climatic cycle (160,000 years). *Atmos. Environ.* **22**, 317–331 (1988).
- 37. Fung, I. et al. Three-dimensional model synthesis of the global methane cycle. *J. Geophys. Res. Atmos.* **96**, 13033–13065 (1991).
- Brook, E. J., Sowers, T. & Orchardo, J. Rapid variations in atmospheric methane concentration during the past 110,000 years. Science 273, 1087–1091 (1996).
- 39. Valdes, P. J., Beerling, D. J. & Johnson, C. E. The ice age methane budget. *Geophys. Res. Lett.* **32**, L02704 (2005).
- 40. Cheng, H. et al. Climate variations of Central Asia on orbital to millennial timescales. *Sci. Rep.* **6**, 36975 (2016).
- 41. Seltzer, A. M. et al. Does δ^{18} O of O_2 record meridional shifts in tropical rainfall? *Climate* **13**, 1323–1338 (2017).
- 42. Wang, X. et al. Millennial-scale precipitation changes in southern Brazil over the past 90,000 years. *Geophys. Res. Lett.* **34**, L23701 (2007).
- 43. Kanner, L. C., Burns, S. J., Cheng, H. & Edwards, R. L. High-latitude forcing of the South American summer monsoon during the last glacial. *Science* **335**, 570–573 (2012).
- Rhodes, R. H. et al. Enhanced tropical methane production in response to iceberg discharge in the North Atlantic. Science 348, 1016–1019 (2015).

- 45. Bard, E., Rostek, F., Turon, J.-L. & Gendreau, S. Hydrological impact of Heinrich events in the subtropical northeast Atlantic. *Science* **289**, 1321–1324 (2000).
- Salgueiro, E. et al. Past circulation along the western Iberian margin: a time slice vision from the last glacial to the Holocene. Quat. Sci. Rev. 106, 316–329 (2014).
- Johnsen, S. J. et al. Oxygen isotope and palaeotemperature records from six Greenland ice-core stations: Camp Century, Dye-3, GRIP, GISP2, Renland and NorthGRIP. J. Quat. Sci. 16, 299–307 (2001).
- Cruz, F. W. et al. Insolation-driven changes in atmospheric circulation over the past 116,000 years in subtropical Brazil. *Nature* 434, 63–66 (2005).
- 49. Berger, A. Long-term variations of daily insolation and Quaternary climatic changes. *J. Atmos. Sci.* **35**, 2362–2367 (1978).
- Clark, P. U. et al. Global climate evolution during the last deglaciation. *Proc. Natl Acad. Sci. USA* 109, E1134–E1142 (2012).
- Thirumalai, K., Clemens, S. C. & Partin, J. W. Methane, monsoons, and modulation of millennial-scale climate. *Geophys. Res. Lett.* 47, e2020GL087613 (2020).
- Clark, P. U., Alley, R. B. & Pollard, D. Northern Hemisphere ice-sheet influences on global climate change. Science 286, 1104–1111 (1999).
- Broecker, W. S. Paleocean circulation during the last deglaciation: a bipolar seesaw? *Paleoceanography* 13, 119–121 (1998).
- Kleinen, T., Gromov, S., Steil, B. & Brovkin, V. Atmospheric methane since the Last Glacial Maximum was driven by wetland sources. Climate 19, 1081–1099 (2023).
- Cheng, H., Sinha, A., Wang, X., Cruz, F. W. & Edwards, R. L.
 The global paleomonsoon as seen through speleothem records from Asia and the Americas. Clim. Dyn. 39, 1045–1062 (2012).
- Buizert, C. et al. Greenland-wide seasonal temperatures during the last deglaciation. Geophys. Res. Lett. 45, 1905–1914 (2018).

- Denton, G. H., Alley, R. B., Comer, G. C. & Broecker, W. S. The role of seasonality in abrupt climate change. Quat. Sci. Rev. 24, 1159–1182 (2005).
- Lambeck, K., Rouby, H., Purcell, A., Sun, Y. & Sambridge, M. Sea level and global ice volumes from the Last Glacial Maximum to the Holocene. Proc. Natl Acad. Sci. USA 111, 15296–15303 (2014).
- 59. Winterfeld, M. et al. Deglacial mobilization of pre-aged terrestrial carbon from degrading permafrost. *Nat. Commun.* **9**, 3666 (2018).
- Hopcroft, P. O., Valdes, P. J. & Kaplan, J. O. Bayesian analysis of the glacial-interglacial methane increase constrained by stable isotopes and Earth system modeling. *Geophys. Res. Lett.* 45, 3653–3663 (2018).
- 61. Buizert, C. et al. Precise interpolar phasing of abrupt climate change during the last ice age. *Nature* **520**, 661–665 (2015).
- 62. Mayewski, P. A. et al. Major features and forcing of high-latitude Northern Hemisphere atmospheric circulation using a 110,000-year-long glaciochemical series. *J. Geophys. Res. Oceans* **102**, 26345–26366 (1997).
- 63. Schüpbach, S. et al. Greenland records of aerosol source and atmospheric lifetime changes from the Eemian to the Holocene. *Nat. Commun.* **9**, 1476 (2018).
- 64. Martin, K. C. et al. Bipolar impact and phasing of Heinrich-type climate variability. *Nature* **617**, 100–104 (2023).

Publisher's note Springer Nature remains neutral with regard to jurisdictional claims in published maps and institutional affiliations.

Springer Nature or its licensor (e.g. a society or other partner) holds exclusive rights to this article under a publishing agreement with the author(s) or other rightsholder(s); author self-archiving of the accepted manuscript version of this article is solely governed by the terms of such publishing agreement and applicable law.

© The Author(s), under exclusive licence to Springer Nature Limited 2023

Methods

Ice-core CH₄ records

To reconstruct the rIPD, samples from the WD ice core were used to measure the Antarctic [CH₄] record across the entire interval (27.5–11.6 ka). The NEEM and GISP2 ice cores were used to generate records of Greenland [CH₄] that broadly represent NH [CH₄]: GISP2 from 27.5 to 14.5 ka and NEEM from 18.5 to 11.6 ka (see Supplementary Information Sections 1 and 2 for measurement details). Each of these NH [CH₄] records were independently synchronized to the longer WD record, which captures mean SH [CH₄]. The overlap of our NEEM and GISP2 [CH₄] records during HS1 allows for the direct comparison of two, independently derived rIPD records.

CH₄ was measured using a vacuum melt/refreeze extraction system for discrete ice-core samples in the Oregon State University ice-core laboratory (Supplementary Information Section 1). Several corrections were made to the raw data^{65,66}. Each measurement was first corrected for instrumental offset (blank) and the differential solubility of CH₄ compared to bulk air components. Our blank correction varies over time $(1\sigma = 2ppb)$, so we use a four-month running mean of daily blanks. The solubility correction is dependent on sample mass, which varied slightly between measurement campaigns. Next, measurements were corrected for gravitational settling in the firn air column. Because the molar mass of CH₄ (16.04 g mol⁻¹) is lighter than air (28.97 g mol⁻¹), [CH₄] is slightly depleted at the lock-in depth relative to the atmosphere 67. This mass-dependent gravitational fractionation is regulated by firn thickness, which varies between warm and cold climate intervals and can be estimated using measurements of δ¹⁵N-N₂ that are corrected for the effect of thermal fractionation⁶⁷. Existing estimates of gravitational fractionation as a function of depth for NEEM⁶¹, GISP2⁶⁸ and WD¹³ were interpolated onto the depths of each sample and used to correct the [CH₄] data. The corrections are summarized by equation (2):

$$[CH4]f = ([CH4]i × S - ([CH4]B × S - [CH4]S)) × G$$
 (2)

where $[CH_4]_f$ is the gravity-, blank- and solubility-corrected $[CH_4]_f$ is the raw value, $[CH_4]_B$ is the measured $[CH_4]$ of the NOAA calibrated standard when introduced over and processed with gas-free ice, $[CH_4]_s$ is the known $[CH_4]$ of the NOAA calibrated standard, S is an empirically determined solubility correction constant and G is the gravitational fractionation factor per unit mass (-1.0003-1.0005) multiplied by molar mass difference between CH_4 and air (12.92 g mol $^{-1}$) 65 . Lastly, we correct for CH_{4xs} and systematic offsets between each campaign and the 2019 reference measurement campaign (see below). Table 1 displays the samples measured to generate our $[CH_4]$ records separated by ice core and year measured (Supplementary Information Section 2), and summarizes the corrections applied to the data.

Correcting for campaign offsets

Offsets between measurement campaigns can be caused by small changes in the analytical system and methods, or drift in the calibrated reference standards. To constrain these offsets, we linearly interpolate the data from each campaign onto the depths of the 2013 WD and NEEM samples for intervals where depth adjacent samples are available (Supplementary Fig. 1). The mean difference between the interpolated and measured [CH4] is used to estimate each campaign offset. We then adjust the [CH4] data to the 2018/2019 measurement campaigns using these offsets so that our GISP2 data agree with ref. 64. Offsets between WD and the two Greenland records were avoided by measuring samples from both cores on the same day.

Overall, the offsets are small (<6 ppb; Table 1) but important to account for, given our IPD approaches 0 ppb at times (Fig. 2). No statistically significant offsets were found between the GISP2 2018 and 2019, WD 2018 and 2019 or the WD 2012 and 2013 data. The WD 2018/2019 data are on average 4 ppb higher than the WD 2012/2013 data. The NEEM 2011 and 2012 data are on average 1.2 ppb lower than the NEEM

2013 data. To match the 2018/2019 data, the 2010–2011 NEEM data were increased by 1.2 ppb to match the 2013 NEEM data, and then all WD and NEEM data from 2010–2013 were increased an additional 4.0 ppb to match the 2018/2019 data. Figure 1 shows the excellent agreement between each measurement campaign for each of the three cores after all corrections were applied.

Correcting for CH_{4xs} in Greenland ice

A recent study³⁵ showed that non-atmospheric CH_4 release during melt-extraction analysis, or CH_{4xs} , could change the measured $[CH_4]$ by up to 40 ppb in Greenland samples with high Ca^{2^+} , a proxy for dust content³⁶. These anomalies are comparable to or sometimes greater than the magnitude of the IPD (Fig. 2), so a correction is essential. We do not observe CH_{4xs} in Antarctic ice, probably because the dust contents are too low for the phenomenon to be detectable³⁵.

We adopt the correction procedure outlined in ref. 35, which uses a multiple melt/refreeze technique to calculate the quantity of CH_{4xs} released during analysis (Supplementary Information Section 3.1). The [CH₄] difference between the first and second melt/refreeze analysis is used to estimate how much CH_{4xs} was released during the first melt/refreeze cycle. This method assumes that the quantities of CH_{4xs} released during the first and second melt/refreeze are equal, although evidence suggests that more is released during the first 35,69 . We find that despite this assumption, our CH_{4xs} correction agrees well with independently derived correction procedures that do not depend on assumptions of the temporal release 69 (Supplementary Information Section 3.3, Supplementary Fig. 4 and Supplementary Table 2).

The linear regression between CH_{4xs} and Ca²⁺ can be used with existing $\text{Ca}^{\text{2+}}$ data to estimate CH_{4xs} when direct measurements thereof are not available. We combine 298 new GISP2 and 29 new NEEM CH_{4xs} measurements with the published 108 GISP2 and 41 NEEM data points in ref. 35 to derive an updated CH_{4xs} -to- Ca^{2+} regression (5.41 ± 0.197 micromoles of CH_{4xs} per mole of Ca^{2+} (mean \pm s.d.), $R^2 = 0.66$; Supplementary Information Section 3.1, Supplementary Table 1; and Supplementary Figs. 2 and 3), which is comparable to ref. 35 (5.16 \pm 0.25, R^2 = 0.78). We find no statistically significant difference between the slopes of the GISP2- and NEEM-derived CH_{4xs}-to-Ca²⁺ regressions (Supplementary Information Section 3.1). We do, however, find significant differences in the slope within the GISP2 regression when measurements are binned by core depth (ice age) and the sample measurement year (Supplementary Information Section 3.1). This variability is noteworthy because the Greenland CH₄ measurements made in this study cover a wide range of ice ages and were measured over the course of nearly a decade. The considerable scatter in the CH_{4xs}-to-Ca²⁺ regression probably stems from the fact that Ca2+ is not the true origin of CH4xx, but only a proxy for processes that are occurring more strongly in Ca²⁺-rich ice⁶⁹. To account for this, we use an uncertainty in the CH_{4xs} correction that incorporates these potential variations in the CH_{4xs}-to-Ca²⁺ regression (Supplementary Information Section 3.1) and find that the added uncertainty does not impact our interpretation of the rIPD (see below).

To make the CH_{4xs} correction, we calculate the absolute molar quantity of CH_4 and Ca^{2+} in each sample and use the linear regression described above to determine the amount of CH_{4xs} expected using the following equation (Supplementary Information Section 3.2):

$$[CH4]c = [CH4]f - \frac{Ca^{2+} \times 10^{9} \times R \times T_{STP} \times C_{xS}}{TAC \times P_{STP}}$$
(3)

where $[CH_4]_c$ is the CH_{4xs} -corrected $[CH_4]$, C_{xs} is the CH_{4xs} correction factor, R is the ideal gas law constant, and T_{STP} and P_{STP} are the standard air temperature and pressure, respectively. TAC is the total air content of the sample, which is calculated using the methods described in ref. 70. The molar Ca^{2+} content of each sample (Ca^{2+}) was calculated by linearly interpolating published $[Ca^{2+}]$ records for NEEM⁶³ and GISP2⁶² onto the depth range of each sample. Figure 2 displays the

 CH_{4xs} -corrected and uncorrected $[CH_4]$ measurements for all GISP2 (Fig. 2a) and NEEM (Fig. 2e) data used in this study, and the $[Ca^{2+}]$ data for each core (Fig. 2b, f).

Ice-core air is offset in depth from ice of the same age because bubble close-off occurs 50–100 m below the ice-sheet surface 71 . Because CH $_{\rm 4xs}$ is determined from ice impurity measurements (Ca $^{2+}$) and gas ages are younger at any depth than ice ages, the CH $_{\rm 4xs}$ corrections impact both stadial and portions of interstadial intervals of the gas record, despite enhanced dust deposition occurring only during stadial periods. Plotting Ca $^{2+}$ on the gas age scale demonstrates this effect (Fig. 2).

Synchronization of Greenland and WD CH₄ records

Gas age chronologies have been independently developed for NEEM 72 , GISP2 68 and WD 13,73 . Because of uncertainties in the gas age models for each core, these chronologies disagree by up to several hundred years (Fig. 1). To calculate the rIPD, synchronizing each [CH $_4$] record onto a single gas age scale is essential. As the interhemispheric mixing time is fast (-1 year) relative to the atmospheric lifetime of CH $_4$ (-10 years), temporal variability in the Greenland and WD [CH $_4$] records should covary nearly perfectly. We synchronize our CH $_{4xs}$ -corrected NEEM and GISP2 [CH $_4$] records to the WD gas age chronology following a Monte Carlo approach 66 .

First, observable [CH₄] changes were used to stratigraphically tie the Greenland gas age scales to the WD2014 gas age scale (32 for NEEM, 31 for GISP2). Next, evenly spaced chronological anchors were chosen to allow the age-depth relationships to change more continuously between the tie points (50 for NEEM, 60 for GISP2). For each of the 10,000 Monte Carlo iterations, a normally distributed random age uncertainty with a standard deviation of 20 years was assigned to the anchors. Additionally, normally distributed analytical error and uncertainty from the CH_{4xs} correction (Supplementary Information Section 3.1) for each data point were included in the synchronization. The iteration that produced the maximum correlation for the linear regression between each Greenland core and WD ($R^2 = 0.995$ for each) was chosen as the new Greenland gas age scale. We stress that our synchronized chronologies make small changes to the existing chronologies, within uncertainties, and we do not recommend their general use in lieu of the existing GISP2 and NEEM timescales 64,68,72. Figure 2a,e shows each of the Greenland [CH₄] records with the WD [CH₄] record on the synchronized WD2014 gas age scale. This comparison illustrates the robust temporal agreement between the synchronized Antarctic and Greenland [CH] records, as well as between NEEM and GISP2 where they overlap.

Calculation of CH₄ rIPD

Measurements of the rIPD are sensitive to measurement noise, outliers, synchronization uncertainty and aliasing of short-term [CH₄] variability by sparse sampling. Additionally, firn smoothing of the atmospheric record via gas diffusion and bubble trapping occurs to differing degrees in each ice core ^{67,74}, resulting in calculated rIPD anomalies during periods of abrupt and short-lived [CH₄] change. To explore the impact of these factors on calculations of the rIPD, we smooth each $[CH_4]$ record using Gaussian smoothing windows ranging from 250 to 750 years (Supplementary Fig. 5). We find that differing degrees of smoothing within this range have little impact on the mean value of the rIPD on millennial scales. Shorter smoothing windows retain unrealistically large centennial-scale rIPD variability that is probably an artefact of differing levels of firn smoothing between each core, synchronization errors, data scatter/outliers and temporal data gaps. An optimal smoothing window of 450 years was chosen because it mitigates those effects without dampening some of the more prominent, multi-centennial-scale and longer features of the rIPD record (Supplementary Fig. 5).

To calculate the smoothed rIPD (Fig. 2), we first linearly interpolate the 450-year smoothed and synchronized Antarctic and Greenland $[CH_4]$ records onto the same evenly spaced, 50-year-resolution

timescale. Next, the interpolated data are used to calculate the rIPD at each interpolated data point. To determine the uncertainty, a smoothed rIPD record is calculated for each iteration of our Monte Carlo synchronization approach, which includes tie point age uncertainties, analytical errors and CH_{4xs} correction uncertainties. For each 50-year time step, the standard deviation of all iterations is calculated and used to create the 95% confidence interval for our rIPD record (Figs. 2d,h and 3a).

Four-box model for reconstructing source distribution

We use a four-box troposphere model 30 to estimate the latitudinal distribution of emissions at each time step of our rIPD reconstruction. The northern tropical (0° – 30° N) and extratropical (30° – 90° N), and southern tropical (0° – 30° S) and extratropical (30° – 90° S) boxes each contain 1 4 of the atmosphere by volume. Four-box, as opposed to two-box, models are advantageous because they account for the higher atmospheric CH₄ sink strength in the tropics and can differentiate between tropical and high-latitude sources across large [CH₄] changes, which are difficult to distinguish using the stable and radioisotopes of CH₄ 11,22 . The mass balance of the model is:

$$\frac{d\mathbf{C}}{dt} = \mathbf{F} + \Omega \times \mathbf{C} \tag{4}$$

where C, F, and dC/dt are vectors representing the atmospheric CH_4 burden (Tg), CH_4 emission strength (Tg yr $^{-1}$), and change in the atmospheric CH_4 burden (Tg) in each box, respectively. Ω is a matrix describing transport between boxes and the CH_4 lifetime in each box. Ω is defined as:

$$\Omega = \begin{bmatrix}
(-\lambda_{NeT} - n_{eT}) & n_{eT} & 0 & 0 \\
n_{eT} & (-\lambda_{NT} - n_{eT} - n_{T}) & n_{T} & 0 \\
0 & n_{T} & (-\lambda_{ST} - n_{eT} - n_{T}) & n_{eT} \\
0 & 0 & n_{eT} & (-\lambda_{SeT} - n_{eT})
\end{bmatrix}$$
(5)

where λ (yr⁻¹) is the inverse of sink strength of each box (indicated by the four subscripts, where N and S indicate north and south, respectively) and n (yr⁻¹) is the inverse of the transport times between tropical and extratropical (eT) and the two tropical (T) boxes. We use the lifetimes used in previous studies of the CH₄ rIPD^{9,12,29,30}, but update the hemispheric and interhemispheric exchange rates, which were originally derived in ref. 30, using the modern atmospheric distribution of sulfur hexafluoride (SF₆) (Supplementary Table 3). SF₆ is ideal for this purpose because of robust atmospheric monitoring in recent decades^{75,76}, long lifetime (>3,200 years) and well-characterized, NH-dominant emissions⁷⁷ (Supplementary Information Section 4).

[CH₄] from 30° S to 90° S (C_s) is well mixed in the modern atmosphere so Antarctic records should record the average [CH₄] in that box. The regions from 30° N to 90° N (C_s) are not homogenously mixed, with [CH₄] increasing with latitude³⁷. To address this, we follow previous studies^{9,29} and modern observations¹, and decrease [CH₄] in our NEEM and GISP2 records by 7% of the Greenland–Antarctica [CH₄] difference to better represent the mean [CH₄] of the northern extratropical box.

With only two data constraints (northern and southern extratropical [CH₄]), the four-box model is under-constrained and requires several assumptions. First, we hold southern extratropical emissions constant at the 1 Tg yr⁻¹ estimated by recent Earth-system modelling studies^{28,54}, and modern inversion studies⁷⁸. Changes in the small emissions of the southern extratropical box during the deglaciation were presumably minimal compared with those in northern extratropical and tropical boxes²⁸. Second, we assume that southern and northern tropical emissions were equal, although the sensitivity of our analyses to this assumption is explored in detail.

Box-model sensitivity tests

The CH₄ rIPD is sensitive to several variables other than the ratio of total tropical to northern extratropical emissions, including atmospheric transport times, CH₄ lifetime and the location of the equatorial barrier to interhemispheric mixing. For example, the strength of the Hadley cell, a major component of interhemispheric mixing, is sensitive to the mean position of tropical rain belts⁷⁹. Changing lifetimes across climate intervals due to varying atmospheric OH concentrations from changing temperature and/or forest biogenic volatile organic compound emissions^{16,80} could have also impacted the rIPD, although several studies suggest that deglacial OH inventories were relatively stable^{24,81-83}. We performed four-box-model sensitivity tests to evaluate if such changes could provide alternative interpretations of the rIPD. Using the average of our GISP2- and NEEM-derived rIPDs across the climate intervals defined by ref. 12 (Supplementary Table 4), we calculate steady-state tropical and northern extratropical emissions¹². We then varied the global mean CH₄ lifetime by $\pm 25\%$, lifetime in the northern extratropical box only by $\pm 25\%$ and the interhemispheric exchange rate by ±50% (Supplementary Figs. 6-8, respectively).

Panels c and f of Supplementary Figs. 6-8 display the ratio of total tropical to northern extratropical emissions for the defined climate intervals. This allows us to calculate the changes in lifetime or interhemispheric exchange rate required to produce our observed rIPD change between climate intervals in the scenario that source distribution (yaxis) remained constant. In principle, changes to lifetime and atmospheric transport are most likely to have occurred at the rapid changes to the climate system during the deglaciation (HS1-YD). We find that the observed 5 percentage point increase of our rIPD across the deglaciation could be caused by a ~4-year increase in global average lifetime (Supplementary Fig. 6), although such a change is currently not supported by Earth-system modelling studies^{16,80}. Increases in northern extratropical CH₄ lifetime (Supplementary Fig. 7c,f), perhaps driven by rising regional biogenic volatile organic compound emissions that would have reduced OH abundance⁸⁰, and changes to interhemispheric exchange rates (Supplementary Fig. 8c,f), each cannot explain the observed deglacial rIPD change. More subtle changes in the rIPD and [CH₄] could plausibly be explained by varying lifetime and interhemispheric exchange rate rather than source distribution (that is, Stadial 2, Stadial 1 and the LGM in the GISP2-derived rIPD), but the large-scale changes during the deglaciation must be driven by changes in the strength and latitudinal distribution of CH₄ emissions.

Another possible and perhaps more influential driver of rIPD $variability\ is\ the\ spatial\ variability\ of\ CH_{4}\ emissions\ within\ the\ tropics$ (30° N-30° S). Tropical emissions, which mainly originate from wetlands, probably shifted latitudinally in response to migrating rainfall patterns during the deglaciation 8,12,39,44. We used our four-box troposphere model to test the impact of such shifts and found that shifting from a scenario with 75% of all tropical emissions in the northern tropics to 75% in the southern tropics decreases the rIPD by 7 percentage points, which is roughly the full range of variability of our calculated rIPD (Supplementary Fig. 9a). These experiments assumed that the equatorial 'barrier' to interhemispheric mixing, determined mainly by the meridional position of the intertropical convergence zone, would not shift with shifting rainfall patterns, although further sensitivity tests that explore this possibility suggest the effect would be small (Supplementary Information Section 5 and Supplementary Fig. 9b). Considering these results, if a northward migration of tropical CH₄ emissions increased the rIPD, our four-box model would incorrectly attribute this increase to enhanced northern extratropical emissions, therefore underestimating tropical emissions and overestimating northern extratropical emissions. In other words, northern extratropical CH₄ emissions may be overestimated during NH interstadials when tropical rain belts, and thus wetland CH₄ emissions, are thought to have

shifted north, with the opposite true for a southward shift during NH stadials. Despite this, we find that the impact that realistic shifts in tropical emissions may have on box-modelled sources is small (at most, $\pm 10~Tg~yr^{-1}$; Supplementary Fig. 10 and Supplementary Information Section 5), and does not hinder our interpretations of the LGM and deglacial CH_4 budget.

Data availability

The [CH $_4$], rIPD and box-model data are published on the Arctic Data Center, US Antarctic Program Data Center (USAP DC) and NOAA National Climatic Data Center. NEEM [CH $_4$], WD [CH $_4$] and GISP2 [CH $_4$] data are publicly available and archived at https://doi.org/10.18739/A2ZC7RW3H and USAP DC 601737, the new CH $_4$,xs data are archived at https://doi.org/10.18739/A2TM7229J, and the GISP2-and NEEM-derived rIPD results and four-box-model output are archived at https://doi.org/10.18739/A2PZ51N77 and USAP DC 601736. Additional GISP2 [CH $_4$] data are archived at https://doi.org/10.18739/A2639K65M. Source data are provided with this paper.

Code availability

The code and data used to calculate the GISP2- and NEEM-derived rIPD records, run the four-box model and plot the results in Figs. 1–3 are archived and publicly available on Github at https://github.com/benryoung23/Riddell-Young_etal_2023.git.

References

- Mitchell, L. E., Brook, E. J., Sowers, T., McConnell, J. R. & Taylor, K. Multidecadal variability of atmospheric methane, 1000–1800 CE. J. Geophys. Res. Biogeosci. 116, G02007 (2011).
- Lee, J. E. et al. An 83 000-year-old ice core from Roosevelt Island, Ross Sea, Antarctica. Climate 16, 1691–1713 (2020).
- 67. Buizert, C. et al. Gas transport in firn: multiple-tracer characterisation and model intercomparison for NEEM, northern Greenland. *Atmos. Chem. Phys.* **12**, 4259–4277 (2012).
- 68. Seierstad, I. K. et al. Consistently dated records from the Greenland GRIP, GISP2 and NGRIP ice cores for the past 104 ka reveal regional millennial-scale δ^{18} O gradients with possible Heinrich event imprint. *Quat. Sci. Rev.* **106**, 29–46 (2014).
- Mühl, M. et al. Methane, ethane, and propane production in Greenland ice core samples and a first isotopic characterization of excess methane. Climate 19, 999–1025 (2023).
- Buizert, C. et al. Antarctic surface temperature and elevation during the Last Glacial Maximum. Science 372, 1097–1101 (2021).
- 71. Schwander, J. & Stauffer, B. Age difference between polar ice and the air trapped in its bubbles. *Nature* **311**, 45–47 (1984).
- Rasmussen, S. O. et al. A first chronology for the North Greenland Eemian Ice Drilling (NEEM) ice core. Climate 9, 2713–2730 (2013).
- Sigl, M. et al. The WAIS Divide deep ice core WD2014 chronology Part 2: Annual-layer counting (0–31 ka BP). Climate 12, 769–786 (2016).
- 74. Johnsen, S. Stable isotope homogenization of polar firn and ice. *Isotopes Impurities Snow Ice* **118**, 210–219 (1977).
- Simmonds, P. G. et al. The increasing atmospheric burden of the greenhouse gas sulfur hexafluoride (SF₆). Atmos. Chem. Phys. 20, 7271–7290 (2020).
- Rigby, M., Manning, A. & Prinn, R. Inversion of long-lived trace gas emissions using combined Eulerian and Lagrangian chemical transport models. *Atmos. Chem. Phys.* 11, 9887–9898 (2011).
- 77. Hall, B. et al. Improving measurements of SF_6 for the study of atmospheric transport and emissions. *Atmos. Meas. Tech.* **4**, 2441–2451 (2011).
- 78. Basu, S. et al. Estimating emissions of methane consistent with atmospheric measurements of methane and $\delta^{13}C$ of methane. Atmos. Chem. Phys. **22**, 15351–15377 (2022).

- Lee, S.-Y., Chiang, J. C. H., Matsumoto, K. & Tokos, K. S. Southern Ocean wind response to North Atlantic cooling and the rise in atmospheric CO₂: modeling perspective and paleoceanographic implications. *Paleoceanography* 26, PA1214 (2011).
- Kaplan, J. O., Folberth, G. & Hauglustaine, D. A. Role of methane and biogenic volatile organic compound sources in late glacial and Holocene fluctuations of atmospheric methane concentrations. *Global Biogeochem. Cycles* 20, GB2016 (2006).
- 81. Levine, J. G., Wolff, E. W., Jones, A. E. & Sime, L. C. The role of atomic chlorine in glacial–interglacial changes in the carbon-13 content of atmospheric methane. *Geophys. Res. Lett.* **38**, L04801 (2011).
- 82. Murray, L. et al. Factors controlling variability in the oxidative capacity of the troposphere since the Last Glacial Maximum. *Atmos. Chem. Phys.* **14**, 3589–3622 (2014).
- 83. Quiquet, A. et al. The relative importance of methane sources and sinks over the last interglacial period and into the last glaciation. *Quat. Sci. Rev.* **112**, 1–16 (2015).

Acknowledgements

This work was supported by the US National Science Foundation (NSF) awards 1702920 (C.B., K.M.), 2102944 (C.B., K.M.) and 0806414 (E.B., C.B., J.R., J.E). The University of Bern gratefully acknowledges financial support by the Swiss National Science Foundation (no. 200020_172506: M.M., J.S., H.F. and 200020B_200328: M.M., J.S., H.F.). We thank the NSF Ice Core Facility (NICF) and the University of Copenhagen for their curation and preparation of the WD/GISP2 and NEEM ice-core samples used in this study, respectively. We also thank

M. L. Kalk for his assistance in methane data measurement at Oregon State University.

Author contributions

Methane data measured by J.R., J.L., J.E., K.M., B.R.-Y., E.B. and C.B.; excess methane data measured by B.R.-Y., K.M., J.L., M.M., J.S. and H.F.; gas age scale synchronization, rIPD calculation and box-model analysis by J.R., B.R.-Y., E.B., J.E. and J.L.; paper preparation by B.R.-Y. and E.B. All authors contributed to the final paper.

Competing interests

The authors declare no competing interests.

Additional information

Supplementary information The online version contains supplementary material available at https://doi.org/10.1038/s41561-023-01332-x.

Correspondence and requests for materials should be addressed to Ben Riddell-Young or Edward Brook.

Peer review information *Nature Geoscience* thanks Victor Brovkin and the other, anonymous, reviewer(s) for their contribution to the peer review of this work. Primary Handling Editors: James Super and Tom Richardson, in collaboration with the *Nature Geoscience* team.

Reprints and permissions information is available at www.nature.com/reprints.